

8-23-2017

Calcium-Mediated Control of S100 Proteins: Allosteric Communication via an Agitator/Signal Blocking Mechanism.

Yiming Xiao

Gary S Shaw

Lars Konermann

Follow this and additional works at: <https://ir.lib.uwo.ca/chempub>

 Part of the [Chemistry Commons](#)

Citation of this paper:

Xiao, Yiming; Shaw, Gary S; and Konermann, Lars, "Calcium-Mediated Control of S100 Proteins: Allosteric Communication via an Agitator/Signal Blocking Mechanism." (2017). *Chemistry Publications*. 260.
<https://ir.lib.uwo.ca/chempub/260>

**Calcium-Mediated Control of S100 Proteins: Allosteric
Communication via an Agitator/Signal Blocking Mechanism**

Yiming Xiao, Gary S. Shaw, and Lars Konermann*

*Department of Chemistry, The University of Western Ontario, London, Ontario,
N6A 5B7, Canada*

* corresponding author

E-mail address of the corresponding author: konerman@uwo.ca

Funding was provided by the Natural Sciences and Engineering Research Council of Canada (DG 217080-2013 to LK) and the Canadian Institutes of Health Research (MOP 93520 to GSS).

Abstract: Allosteric proteins possess dynamically coupled residues for the propagation of input signals to distant target binding sites. The input signals usually correspond to “effector is present” or “effector is not present”. Many aspects of allosteric regulation remain incompletely understood. This work focused on S100A11, a dimeric EF-hand protein with two hydrophobic target binding sites. An annexin peptide (Ax) served as target. Target binding is allosterically controlled by Ca^{2+} over a distance of ~ 26 Å. Ca^{2+} promotes formation of a $[\text{Ca}_4 \text{S100 Ax}_2]$ complex, where the Ax peptides are accommodated between helices III/IV and III'/IV'. Without Ca^{2+} these binding sites are closed, precluding interactions with Ax. The allosteric mechanism was probed by microsecond MD simulations in explicit water, complemented by hydrogen exchange mass spectrometry (HDX/MS). Consistent with experimental data, MD runs in the absence of Ca^{2+} and Ax culminated in target binding site closure. In simulations on $[\text{Ca}_4 \text{S100}]$ the target binding sites remained open. These results capture the essence of allosteric control, revealing how Ca^{2+} prevents binding site closure. Both HDX/MS and MD data showed that the metalation sites become more dynamic after Ca^{2+} loss. However, these enhanced dynamics do not represent the primary trigger of the allosteric cascade. Instead, a labile salt bridge acts as an incessantly active “agitator” that destabilizes the packing of adjacent residues, causing a domino chain of events that culminates in target binding site closure. This agitator represents the starting point of the allosteric signal propagation pathway. Ca^{2+} binding rigidifies elements along this pathway, thereby blocking signal transmission. This blocking mechanism does not conform to the commonly held view that allosteric communication pathways generally originate at the sites where effectors interact with the protein.

Introduction

Signaling proteins possess specific sites for binding their biological targets, such as nucleic acids or other proteins. Many of these interactions are controlled by allosteric effectors,¹⁻³ i.e., species that modulate the protein's target affinity by interacting with locations remote from the target binding site.⁴⁻⁶ The dysregulation of allosteric interactions can lead to cancer and other diseases.⁷ Also, allostery is a central element of drug action mechanisms.^{8,9}

Classical models of allostery envision that effector binding triggers conformational changes that cause distant target binding sites to open or close.^{1,2,4} Recent studies have expanded this view by emphasizing the role of conformational dynamics.¹⁰⁻¹² For example, it has been proposed that proteins fluctuate between co-existing conformers, and that allosteric effectors shift these equilibria towards structures with higher or lower target affinities.^{6,13-16} Regardless of the exact mechanism, allostery requires the transmission of signals to target binding sites, often over tens of Ångstroms.^{11,15} Such signals travel along dynamically coupled residues.^{16,18,19} Allosteric signal propagation pathways have been identified on the basis of mutational¹⁷ and evolutionary data,¹⁸ NMR spectroscopy,^{16,19-22} X-ray crystallography,^{1,23,24} molecular dynamics (MD) simulations,^{6,9,25-30} and hydrogen-deuterium exchange (HDX) mass spectrometry (MS).³¹⁻³⁴ Even after allosteric pathways have been identified, however, the exact mechanisms by which remote sites communicate often remains unclear.

Calcium represents one of the most common allosteric regulators. The intracellular Ca^{2+} concentration under resting conditions is low, but it rises sharply following stimuli that cause the opening of membrane channels. This Ca^{2+} influx can activate signaling proteins, allowing them to bind their targets. Subsequent deactivation relies on membrane pumps that return the calcium concentration to its resting value, such that protein-target complexes dissociate again.³⁵

A particularly important group of calcium-dependent signaling proteins is the S100 family which is involved in numerous functions and diseases.³⁶⁻³⁸ Here we focus on S100A11, a typical homo-dimeric S100 family member that binds four Ca^{2+} and two target proteins.³⁹ One of these targets^{40,41} is annexin A2, a protein that interacts with the plasma membrane.⁴² Calcium-loaded S100A11 can link two annexin A2 chains, thereby forming a complex required for membrane repair, specifically in cancer cells.^{43,44}

Each S100A11 subunit comprises four helices. The helix III/IV loop forms a high-affinity EF-hand calcium binding site. A lower affinity pseudo EF-hand is formed by the helix I/II loop (Figure 1a).^{35,45} In the Ca^{2+} -bound form helices III/IV adopt a near-perpendicular orientation that results in an open target binding site. Figure 1b shows the structure of S100A11 with four Ca^{2+} and two annexin peptides.³⁹ We will refer to this complex as $[\text{Ca}_4 \text{ S100 Ax}_2]$. Square brackets indicate components that are bound in a complex, the annexin peptide is denoted as Ax, and “A11” is omitted to streamline the notation. In apo-S100, helices III/IV are in a more antiparallel orientation, resulting in a closed target binding site that precludes interactions with Ax (Figure 1c).⁴⁶ Similar transitions take place for many other Ca^{2+} -dependent proteins.^{35,47}

The cooperative nature of allosteric regulation can be illustrated by using a thermodynamic cycle.⁴⁸⁻⁵⁰ Figure 1d considers two possible pathways for the conversion of apo-S100 to $[\text{Ca}_4 \text{ S100 Ax}_2]$. Steps 1 and 2 represents the “canonical” scenario where metalation takes place first, followed by Ax binding. In this case calcium enhances the protein’s Ax binding affinity by $\Delta\Delta G^\circ = -RT \ln C_{Ca}$, where the factor $C_{Ca} > 1$ reflects how the Ax binding equilibrium responds to the presence of calcium.^{48,49} Alternatively, one may consider a pathway where Ax binds first (step 3), followed by metalation (step 4). In this second scenario, Ax enhances the metal binding affinity by $\Delta\Delta G^\circ = -RT \ln C_{Ax}$.^{48,49,51} Thus, Ca^{2+} binding enhances the target affinity, and target binding enhances the Ca^{2+} affinity. This implies that allosteric signals must be able to travel from effector

sites to target binding sites and *vice versa*. Both scenarios are associated with the same affinity enhancement, because $C_{Ca} = C_{Ax} = C$.⁴⁸⁻⁵⁰ For the system considered here $C \approx 10$.^{46,51-53}

A number of studies have explored Ca^{2+} -dependent allosteric effects in S100 family members and other EF-hand proteins^{35,54-57} The mechanism by which metal binding sites control target binding sites over a substantial distance nonetheless remains poorly understood.^{46,58} For the system considered here, this distance is roughly 26 Å (measured from the center of an Ax helix to the EF-hand Ca^{2+} in the same subunit)³⁹ Simply speaking, the field is dominated by the view that calcium loss enhances the conformational freedom of the EF- and pseudo EF-hands, and that this increased flexibility triggers a sequence of events that culminates in target binding site closure.

Here we scrutinized the mechanism of S100 allosteric regulation by employing microsecond molecular dynamics (MD) simulations in explicit water, complemented by hydrogen/deuterium exchange mass spectrometry (HDX/MS). Protein structure and dynamics were probed in the presence/absence of calcium and Ax, corresponding to the complexes [Ca₄ S100 Ax₂], [Ca₄ S100], [S100 Ax₂] and apo-S100. Our data reveal an unexpected regulatory mechanism. Closure of the target binding site represents the culmination of an allosteric cascade that does *not* originate at the metalation sites. Instead, binding site closure is triggered by structural perturbations emanating from a labile salt bridge that acts as incessantly active “agitator”. Bound calcium stabilizes the target binding sites in an open conformation by blocking allosteric signals produced by the agitator. To our knowledge, the current work marks the first time that such an allosteric mechanism has been documented.

Methods

Proteins and Reagents. Rabbit S100A11 was expressed and purified as described.^{46,59,60} As in previous work,⁶¹ a C9S variant was used to avoid inappropriate disulfide formation. The expected monomer mass (11281 Da) was verified by MS (11281.5 ± 1) Da. Ax (acetyl-STVHEILSKLSLEGD) was synthesized by BioBasic (Markham, ON). This peptide was used because of its higher solubility and binding affinity,⁶¹ compared to the annexin A1 peptide in the 1QLS X-ray structure.³⁹ D₂O (Aldrich, St. Louis, MO), KCl (Caledon, Georgetown, ON), HEPES, EDTA (Sigma), CaCl₂, and HCl (Caledon) were used as received.

HDX Mass Spectrometry. Deuteration was performed at 23 ± 1 °C in 90% D₂O, 50 mM KCl, 20 mM HEPES, at a pH meter reading of 7.1. These solution conditions were chosen to ensure consistency with previous NMR studies, which demonstrated that background electrolyte concentrations $\gg 50$ mM can interfere with Ca²⁺ binding.^{46,61} The protein concentration was 2.5 μ M (as dimer). Other components were added as needed, i.e., 5 mM CaCl₂ for experiments conducted in the presence of Ca²⁺, 0.2 mM EDTA for Ca²⁺-free samples, and with or without 70 μ M Ax. All concentrations refer to the final values under HDX conditions. From published dissociation constants it can be estimated that $\sim 99.5\%$ of the metalation sites were occupied in the Ca²⁺ containing solutions,⁶² and $\sim 95\%$ of the protein was bound to Ax in [Ca₄ S100 Ax₂] samples.⁶¹ 100 μ L aliquots were removed at various time points between 1 min and 2 h after initiation of labeling. The aliquots were quenched to pH 2.3 by addition of HCl on ice, flash frozen in liquid nitrogen, and stored at -80 °C. The aliquots were thawed to $\sim 0^\circ\text{C}$ and injected into an HDX nanoACQUITY UPLC⁶³ (Waters, Milford, MA). Digestion was performed on a 2.1 mm \times 30 mm POROS pepsin column (Applied Biosystems, Carlsbad, CA) at 15°C. Peptides were

trapped on a Waters BEH C18 (1.7 μm , 2.1 \times 5 mm) column, and separated on a BEH C18 (1.7 μm , 1 \times 100 mm) column using a water/acetonitrile gradient with 0.1% formic acid at 40 $\mu\text{L min}^{-1}$. Data analysis focused on 17 peptides that cover the sequence in a contiguous fashion (Supporting Figure S1). Peptide masses were measured on a Waters Synapt G2 Q-TOF mass spectrometer. Peptide identities were confirmed by MS/MS. For correction of in-exchange, zero time point controls (m_0) were performed by exposing the protein to labeling buffer under quench conditions. Fully exchanged controls (m_{100}) were prepared by incubation in labeling buffer at pH 2.4 and 37 $^{\circ}\text{C}$ for 24 h. HDX temporal profiles were obtained from centroid mass values at time t , m_t , obtained by DynamX 3.0 (Waters). Deuteration levels are reported as *percent deuteration* = $(m_t - m_0)/(m_{100} - m_0)$, where m_t represented the centroid mass of a peptide at time t . All samples displayed uncorrelated HDX with gradual shifts of the isotope envelopes to higher mass, as commonly seen in the EX2 regime.⁶⁴ All HDX data represent an average of triplicate measurements. Error bars indicate standard deviations.

MD Simulations. MD simulations were conducted using GROMACS 5 with GPU acceleration⁶⁵ at 298 K. The coordinates of human S100A11 bound to four Ca^{2+} and two annexin peptides (pdb file 1QLS)³⁹ served as starting structure for all runs. Human S100A11 and the rabbit variant used in our HDX/MS experiments have slightly different sequences (84% sequence identity). To ensure that MD results and HDX/MS data were directly comparable we swapped several amino acids in the 1QLS starting structure using the mutagenesis and sculpting routines implemented in PyMol (Schrödinger), as detailed in Supporting Figure S2. Similarly, the annexin A1 peptide of the 1QLS structure was transformed to the homologous Ax sequence. Simulations were conducted using the CHARMM 36 force field⁶⁶ with TIP3P water.⁶⁷ This combination has previously been shown to yield reliable folding and equilibrium dynamics.⁶⁸ The protein was placed in a periodic box with a

minimum distance of 7 Å between protein and the box surface. ~8000 water molecules were added, as well as 70 mM K⁺ and Cl⁻, plus additional ions to ensure charge neutrality. After one round of energy minimization atomic velocities were initiated from a Maxwell-Boltzmann distribution with random seeds. This was followed by 100 ps NVT and NPT equilibration runs. Production runs were conducted with a 2 fs time step, using a Parrinello-Rahman barostat and Berendsen thermostat.⁶⁹ Bonds were constrained by the linear constraint solver algorithm.⁷⁰ Short-range electrostatic and van der Waals cutoffs were set to 10 Å. Long-range electrostatics were treated using Particle Mesh Ewald summation,⁷¹ with PME order = 4 and Fourier spacing = 0.16 nm. Two independent 1 μs simulations were conducted for each of the conditions [Ca₄ S100 Ax₂], [Ca₄ S100], [S100 Ax₂] and apo-S100, for a total of eight 1 μs runs. Major structural changes were observed only for apo-S100, prompting us to perform an additional 200 ns run for this species to verify reproducibility. All repeat runs employed slightly different starting coordinates and initial velocities.

Results and Discussion

Molecular Dynamics Simulations. We conducted 1 μs MD simulations on [Ca₄ S100 Ax₂], [Ca₄ S100], [S100 Ax₂], and apo-S100. Using the [Ca₄ S100 Ax₂] X-ray coordinates³⁹ as starting point, structural changes were triggered by removal of calcium and/or Ax. All simulations converged towards relaxed (meta)stable conformers within ~0.5 μs (Supporting Figure S3). As a benchmark, we verified that [Ca₄ S100 Ax₂] maintained a conformation close to the initial X-ray structure (Figure 2a). Runs without calcium and Ax produced structures consistent with the apo-S100 NMR coordinates (Figure 2b). These tests confirm that the MD conditions used are adequate.

Target binding site conformations can be characterized by examining the orientation of helices III/IV (Figure 2c). For helix angles of $\sim 115^\circ$ or less the binding sites are open and capable of accommodating Ax. Larger values (around 155°) represent closed binding sites.^{39,46,72} Most S100 structural studies^{39,46,72} reported the same angle for both subunits in the homodimer due to symmetry constraints imposed during analysis⁷³ (Figure 2c, gray bars). However, in solution⁷⁴ and in our unconstrained MD simulations the helix III/IV and helix III'/IV' angles will not be identical. Figure 2c therefore displays two angles for each MD structure. Runs for [Ca₄ S100 Ax₂] and [Ca₄ S100] maintained open binding sites with angles close to those of the corresponding experimental structures.^{39,72} Experimental data for [S100 Ax₂] are not available; the two MD runs conducted for this species culminated in somewhat different outcomes. In the first instance both binding sites stayed open. The second [S100 Ax₂] run yielded dissimilar angles of $\sim 85^\circ$ for helices III/IV (open), and $\sim 144^\circ$ for III'/IV' (closed). Finally, the simulated apo-S100 angles all corresponded to closed binding sites (Figure 2b), as noted above.⁴⁶

Details of MD Structures. Figure 3 provides a closer look at examples of $t = 1 \mu\text{s}$ MD structures, using a layout consistent with that of Figure 1d. [Ca₄ S100 Ax₂] exhibited a globular fold with a well-developed hydrophobic core (Figure 3a). Both Ax peptides remained tightly associated with the hydrophobic target binding pockets. The EF-hand calcium binding loops at the protein surface were firmly rooted in the core via nonpolar anchor residues (L63 and L71). Each EF-hand was in close contact with an intricately packed “shoulder” consisting of D57/K32/M60/L71. In this shoulder D57 and K32 were connected by a salt bridge, while K32, M60, and L71 were linked by close hydrophobic contacts. The K32-D57 salt bridge as well as the adjacent packing contacts are highly conserved in S100 proteins.⁷⁴ It may seem counter-intuitive to have lysine (a “hydrophilic”

residue) involved in hydrophobic packing, but motifs of this type are common, as governed by the aliphatic nature of the $C_\alpha H-CH_2-CH_2-CH_2-CH_2-$ moiety in lysine.⁷⁵

[S100 Ax₂] showed partial disruption of the D57/K32/M60/L71 shoulder (Figure 3b). For the structure exemplified in Figure 3, only one of the target binding sites retained tight Ax contacts. The second site adopted a closed structure, while the corresponding Ax peptide remained loosely associated via residual nonpolar contacts (colored in Figure 3b). Closure of this binding sites was a gradual process that extended over $\sim 0.5 \mu s$ (Supporting Figure S4A (q)). The perturbed target interactions suggest that the corresponding Ax peptide is poised to separate from the complex, although dissociation did not take place on the time scale of our simulations. Still, the [S100 Ax₂] MD structure clearly represents an intermediate en route towards target-free apo-S100.

Except for the absence of Ax, the [Ca₄ S100] 1 μs structure was very similar to that of [Ca₄ S100 Ax₂]. Both possess open target binding sites and intact D57/K32/M60/L71 shoulders (Figure 3c). This is different from apo-S100, where target binding site closure in both subunits was associated with complete disintegration of the D57/K32/M60/L71 shoulders (Figure 3d).

Allosteric Control of Target Binding Sites. Our MD data capture a central aspect of calcium-mediated allosteric control, i.e., the fact that in apo-S100 the target binding sites collapse to a closed conformation that cannot bind Ax (Figure 3d). This is in contrast to [Ca₄ S100] where calcium maintains open target binding sites that are primed for Ax interactions (Figure 3c).

For deciphering the mechanism of allostery it is essential to identify the driving force for binding site closure. This event is not associated with the formation of stable salt bridges. Also, changes in H-bonding are minor (Supporting Figure S5).^{54,55} However, [Ca₄ S100] possesses numerous solvent exposed nonpolar residues in the target binding sites (Figure 4a). Binding site closure dramatically reduces the accessibility of these residues and allows them to form

hydrophobic contacts (A45, F46, V55, M59, L63, A86, F91, Figure 4b). Hence, the main driving force for binding site closure is the hydrophobic effect (Figure 4a, b).⁷⁶⁻⁷⁹ At the risk of sounding naïve, we point out parallels between this [Ca₄ S100] → apo-S100 closure (Figure 4a, b) and another “allosteric” process, i.e., a spring-loaded mouse trap that snaps close after a rodent pulls at the bait. Bait movements do *not* provide the driving force for the closure event. Instead, pulling at the bait triggers the release of energy stored in the spring. Analogously, Ca²⁺ loss does *not* provide the driving force for binding site closure. Instead, Ca²⁺ loss triggers the release of free energy associated with hydrophobic collapse of the binding site (Figure 4b).⁷⁷⁻⁷⁹ Within this picture, the exposed nonpolar sites in [Ca₄ S100] serve a purpose analogous to that of the spring in the trap. This digression prompts two questions: (i) How does the presence of Ca²⁺ prevent binding site closure? (ii) How does the absence of Ca²⁺ trigger binding site closure? Both can be addressed by examining the temporal behavior of selected atom distances (Figure 4c), with primary focus on [Ca₄ S100] and apo-S100 (Figure 4d-u).

Our simulations reveal that the metalation sites became more dynamic after calcium loss, exemplified by the D68-F73 distance fluctuations in Figure 4d/j/p. F73 represents a quasi-stationary reference point, while D68 is in the center of the EF-hand. Importantly, the enhanced D68 dynamics are not directly correlated with target binding site closure events (Figure 4n, t). This lack of correlation reflects the fact that much of the EF-hand is only weakly coupled to the protein core (Figure 5a). The same is true for the pseudo EF-hand loops, which extend far into the solvent (Figure 4a, b). Thus, the problem has to be investigated from a broader perspective, by also examining events taking place elsewhere in the protein.

The egregious exposure of hydrophobic residues in the [Ca₄ S100] target binding sites can be maintained because of favorable nonpolar packing between helices II and III adjacent to the EF-hands. This hydrophobic cluster includes L63, it is capped off by the D57/K32/M60/L71

shoulder, and it suspends helix III in the open conformation (Figure 5a). Surprisingly, in [Ca₄ S100] the shoulder can undergo large perturbations *without* triggering irreversible binding site closure, exemplified by events between $t = 50$ and 80 ns (Figure 4e-i). During this time the K32-D57 salt bridge underwent dissociation, M60 moved away from L71, L63/L71 drifted apart, and the binding site began to close (evident from a decreasing V55-A86 distance, Figure 4h). A snapshot taken at $t = 70$ ns illustrates the severity of these perturbations, which even included disruption of D64 and N66 metal ligation in the EF-hand (Figure 5b). Remarkably, these events stalled at $t \approx 70$ ns. Instead of closing all the way, the binding site returned to the fully open state, and the D57/K32/M60/L71 shoulder underwent re-assembly (Figure 4e-h). The observed behavior suggests that a key event is not permitted to happen in [Ca₄ S100], which would otherwise allow binding site closure to go to completion.

Our data suggest that binding site closure in [Ca₄ S100] is prevented by a lack of L63-F73 distance fluctuations (more support for this assertion is provided in the next paragraph). As noted, L63 represents an EF-hand anchor. F73 remains virtually stationary under all conditions. In [Ca₄ S100] L63 and F73 are locked at a distance around 11 Å (Figure 4i). The invariability of this distance results from constraints imposed by calcium-protein contacts in the EF-hand (Figure 5a). In summary, in [Ca₄ S100] hydrophobic packing of the shoulder/EF-hand region suspends helix III in the open state. This arrangement is stabilized by L63-F73 distance constraints that arise from Ca²⁺-induced rigidification of adjacent residues (Figures 1a, 5a). Thus, calcium ensures that perturbations in the shoulder get “blocked” as they propagate from K32 towards the core (note the gradually diminishing amplitude at $t \approx 70$ ns when going from Figure 4e to 4i). In this way calcium prevents irreversible binding site closure in [Ca₄ S100]. Another example of such a blocked propagation process, observed in an independent [Ca₄ S100] run, is highlighted in Supporting Figure S6.

In apo-S100 all closing transitions were irreversible. Although different MD runs showed slightly different sequences, each closing event was associated with major L63-F73 distance fluctuations and a subsequent L63-F73 distance increase from ~ 11 Å to ~ 14 Å. We will highlight two runs in more detail. In the first example disassembly of the shoulder took place gradually over ~ 40 ns (Figure 4k-m). During this time the K32-D57 salt bridge dissociated and M60 moved away from L71. The L63-L71 distance underwent a major fluctuation which extended to L63-F73. The latter event triggered closure of the target binding site at $t \approx 25$ ns (dashed line, Figure 4n). In another apo-S100 run (Figure 4q-u) dissociation of the K32-D57 salt bridge took place within the first few nanoseconds, followed by repositioning of M60. Alterations in L63-L71 distance were minor, but a change in L63-F73 distance within the initial 10 ns allowed the target binding site to move into a semi-closed state. At $t \approx 60$ ns the binding site closed completely, while simultaneously the L63-F73 distance increased to ~ 14 Å. Our data suggest that L63-F73 distance *fluctuations* are the key prerequisite for target binding site closure, rather than the L63-F73 distance increase from 11 Å to 14 Å. This is evident from the fact that at the transition midpoints of Figures 4o,u the L63-F73 distances are still relatively small, around 12 Å. Also, after the binding sites had closed, the L63-F73 distance could temporarily return from 14 Å back to 12 Å (Supporting Figure S4B, panel x, chain A, 300-600 ns). Numerous other distances were scrutinized, but no events were correlated with binding site closure as clearly as the L63/F73 behavior.

We conclude that target binding site closure in apo-S100 is the result of a domino cascade that starts with disintegration of the D57/K32/M60/L71 shoulder. The labile K32-D57 salt bridge represents the primary “agitator”. Dissociation of this salt bridge is followed by M60 swinging away from L71. In the absence of Ca^{2+} the hydrophobic packing of residues next to L63 and F73 is not stabilized by EF-hand mediated rigidification, allowing the formation of extensive new

hydrophobic contacts as the target binding sites close (Figure 4b). Complete 1 μ s trajectories for all four conditions are provided in Supporting Figure S4. Those data confirm a high propensity of the K32-D57 salt bridge to undergo reversible dissociation even for [Ca₄ S100 Ax₂], in line with the labile nature of this contact in [Ca₄ S100].

The apo-S100 closing cascades highlighted in Figure 4 refer to collapse of the first binding site in the dimer. In both instances the collapse of the second site took place ca. 70 ns after the first one. Those subsequent closure events also required L63-F73 distance fluctuations (Supporting Figure S7). In a third apo-S100 run both sites underwent initial closure roughly simultaneously around 25 ns, but chain A settled into a fully relaxed closed state only after ~450 ns (Supporting Figures S4B, S7). Taken together, these observations suggest that closure events affecting the two binding sites within a S100 dimer are not directly coupled to one another.

Probing Calcium and Target Binding by HDX/MS. Our MD simulations successfully captured ns - μ s events associated with allosteric control. However, conformational fluctuations in solution can extend to time scales that are orders of magnitude longer,⁸⁰ stretching into realms that are inaccessible by MD techniques.^{68,81} A comprehensive characterization of protein dynamics thus requires the application of complementary approaches that report on dynamics taking place on a wider time range. Continuous labeling HDX/MS is well suited for this purpose. This technique monitors the deuteration of backbone amides. HDX/MS reports on protein dynamics because NH deuteration is mediated by H-bond fluctuations that are coupled to backbone motions. EX2 rate constants can be expressed as $k_{\text{HDX}} = (k_{\text{op}}/k_{\text{cl}}) k_{\text{ch}}$, where k_{op} and k_{cl} are H-bond opening/closing rate constants, while k_{ch} reflects deuteration of unprotected sites.⁸² Deuteration kinetics thus provide a cumulative picture of H-bond fluctuations that occur on time scales of sub-microseconds to seconds and beyond.⁸⁰ To be clear, the use of HDX/MS in our experiments does not imply that

changes in H-bonding constitute the mechanistic foundation of S100 allostery. Rather, as noted throughout the text, rearrangements of hydrophobic moieties were identified as the primary factor for signal propagation and binding site closure (Figure 4). HDX/MS nonetheless provides a window into allosteric events, because different allosteric switching states exhibit different HDX fingerprints.

HDX/MS conditions were designed to mimic those of the MD investigations. Comparison of the deuteration kinetics for [Ca₄ S100 Ax₂], [Ca₄ S100], [S100 Ax₂] and apo-S100 reveals that the addition of calcium and/or Ax solicits highly complex responses throughout the protein (Supporting Figures S8, S9). These range from stabilizing effects to local destabilization. Similarly convoluted HDX patterns have been reported for other allosteric proteins.⁸³⁻⁸⁶ The HDX/MS data are also consistent with NMR-based HDX experiments on the apo and Ca₄ forms of S100B.⁸⁷

The most pertinent HDX/MS results are summarized in Figure 6. Some regions were highly protected under all conditions, exemplified by peptide 14-17 which is part of the tightly packed core (Figure 6a). Other segments, such as the N- and C-termini were completely deuterated already at the earliest time point, attesting to their flexible nature without stable H-bonds (Figure 6d). Calcium and Ax reduced the deuteration of the pseudo EF-hand in an additive fashion, demonstrating that both binding partners stabilize the H-bonding network in this area (Figure 6b). The EF-hand showed pronounced synergy between calcium and Ax-mediated stabilization. This region exhibited complete deuteration in apo-S100, some protection in [Ca₄ S100], and dramatically reduced HDX in [Ca₄ S100 Ax₂] (Figure 6c). Unlike for the pseudo EF-hand, Ax alone did not cause significant changes in the EF-hand (Figures 6b and 6c).

The discussion of our MD data in the preceding sections implicitly focused on allosteric control along steps 1 and 2 of the thermodynamic cycle of Figure 1d, where Ca²⁺ facilitates Ax binding by preventing closure of the target binding site. The calcium-mediated Ax affinity

enhancement is $\Delta\Delta G^\circ = -RT \ln C$. The HDX protection patterns of Figure 6b and 6c reflect the flipside of allosteric control, i.e., the fact that Ax governs the calcium affinity in accordance with steps 3 and 4 of Figure 1d.⁴⁸⁻⁵⁰ Deuteration level changes in [Ca₄ S100 Ax₂] relative to [Ca₄ S100] are consistent with Ax-mediated calcium binding enhancement, as Ax allosterically stabilizes the H-bonding network in all four calcium-binding sites. This is evident from the observation that HDX levels of the metalation sites are lower when Ax and Ca²⁺ are present together, than when only Ca²⁺ is bound (Figure 6b, 6c). Our MD data reveal the basis of this allosteric reciprocity.⁵⁰ The presence of Ax in [S100 Ax₂] ensures that several residues close to the calcium binding region maintain a “holo-like” orientation, e.g., the D57/K32/M60/L71 shoulder does not get disrupted to the same extent as in apo-S100 (Figure 3b and 3d). Ax enhances the calcium binding affinity by $\Delta\Delta G^\circ = -RT \ln C$. Earlier work suggests that $C \approx 10$,^{46,51-53} such that the allosteric stabilization associated with either pathway (1/2 or 3/4 in Figure 1d) is roughly 6 kJ mol⁻¹.

HDX Experiments and MD-Derived H-Bond Patterns. Classical models of backbone NH deuteration envision that the transient disruption of amide H-bonds is the sole determinant of HDX rates.⁸⁸ Recent studies suggest that other factors such as solvent accessibility and electrostatics may also exert some influence, but the central role of H-bond fluctuations remains undisputed.^{80,81,89,90} It is interesting to compare experimental deuteration values with MD-derived H-bonding patterns. Figure 7 shows HDX percentages measured after 10 minutes of labeling. Also shown are MD data reflecting the fraction of time that each backbone amide is H-bonded. This H-bonding analysis takes into account all possible protein acceptor sites, including carboxylates which participate in NH contacts in the calcium binding loops (Supporting Figure S4). Readers are reminded that the MD data only reflect a 1 μ s time window, while the experimental data report on

fluctuations that extend to seconds and beyond.⁸⁰ HDX/MS can therefore pinpoint regions undergoing slow conformational dynamics that go undetected in MD simulations.

Simulated H-bond percentages and experimental HDX levels in Figure 7 are remarkably consistent throughout much of the sequence range. All four conditions resulted in weak H-bonding (high HDX levels) at the termini and inter-helical loops. H-bonds in helical regions tended to be more stable (with lower HDX levels). In the EF-hand around residue 70 simulated H-bonds were well developed (with low HDX values) for [Ca₄ S100 Ax₂] and [Ca₄ S100]. Less pronounced H-bonding (and elevated HDX levels) were encountered in this region for [S100 Ax₂] and apo-S100. Thus, both experiments and MD simulations revealed that calcium significantly stabilizes H-bonds in the vicinity of the EF-hands.

Diverging behavior between simulated H-bond patterns and experimental HDX data were observed in a few instances. The double-headed arrows in Figure 7 highlight segments where simulations indicate well-developed H-bonds, while the experimental HDX data show a lack of protection. This behavior was observed around residue 88 close to the center of helix IV for all conditions, with the exception of apo-S100 (Figure 7d). Similar effects were also encountered for [Ca₄ S100] and apo-S100 in the vicinity of residue 62 (Figures 7b, 7d). Thus, regions marked with double-headed arrows undergo H-bond opening/closing transitions that take place on time scales much slower than the μ s regime explored in our simulations. Overall, Figure 7 nonetheless demonstrates a high level of consistency between simulated and measured H-bond properties.

Conclusions

Allosteric proteins possess communication pathways that allow the transfer of signals between remote sites along dynamically coupled residues.^{1,6,9,11,15-21,23-34,91} Previous studies implicitly

assumed that the starting point of any given communication pathway coincides with an effector binding site. Hence, it is commonly thought that effector binding (or loss) constitutes the initial trigger event that subsequently propagates via a domino-like cascade, culminating in conformational changes elsewhere in the protein. Figure 8a schematically illustrates this classical paradigm, assuming a scenario where the bound effector promotes an open target binding site. Loss of the effector (magenta) triggers a cascade of events along an allosteric pathway (blue), ultimately causing closure of the target binding site (red).

Figure 8a represents a reasonable description of allosteric regulation for many proteins, as suggested by similar cartoons in numerous reviews and biochemistry texts.^{8,92,93} However, calcium-mediated S100 control follows a different mechanism, as uncovered in this work. Closure of the target binding site is the result of an allosteric cascade that is *not* triggered by the effector. Instead, the K32-D57 salt bridge acts as an “agitator” that is labile and destabilizes packing interactions of adjacent residues. Random thermal fluctuations of this agitator represent the initial trigger of the allosteric cascade. The agitator is coupled to the target binding site by dynamically linked residues that allow the initial perturbation to propagate, resulting in closure of the binding site (Figure 8b). The effector (calcium) acts by blocking signals emanating from the agitator, i.e., by interfering with the transmission of allosteric signals (Figure 8c). This blockage is achieved by damping the fluctuations of residues involved in the allosteric cascade.

Figure 8d summarizes details of the signal blocking mechanism uncovered in this study. In [Ca₄ S100] helix III is suspended in the open conformation by packing interactions within the D57/K32/M60/L71 shoulder. These interactions extend to adjacent hydrophobic sites such as L63 and L71, and to helix II which is positioned behind helix III (Figure 8d, left hand side). The top center panel of Figure 8d illustrates events taking place upon calcium loss from [Ca₄ S100]. The K32/D57 salt bridge is labile and undergoes dissociation/re-association transitions which represent

the initial trigger event (marked as “1” in the allosteric cascade of Figure 8d). This agitation propagates via disruption of K32/M60 (“2”) and M60/L71 (“3”) interactions. The breakdown of packing interactions becomes irreversible once L63/F73 undergo a major distance fluctuation (“4”), allowing helix III to swing downward such that the target binding site closes (“5”). This closing event is driven by the burial of hydrophobic sites between helices III and IV. If calcium is present (Figure 8d, bottom center) structural disturbances generated at the K32-D57 agitator cannot proceed beyond L71, because metal-protein contacts in the EF-hand rigidify the L63-F73 distance. Hence, the allosteric cascade comes to a halt, and the target binding site remains open.

There is prior evidence for scenarios where allosteric pathways are affected by interactions with other communication channels. For example, the outcome of effector binding can be altered by affinity modulators, efficacy modulators, agonists, or antagonists.^{8,92,93} The current work further expands the spectrum of possible branched signaling scenarios. We uncover a mechanism where a constitutively active agitator communicates with a remote target binding site. Only in the absence of calcium does the resulting signal cascade cause binding site closure, while bound calcium dampens the motion of key residues along the allosteric pathway. Thus, the effector (calcium) works by blocking the information flow between agitator and target binding site.

In general terms, we propose that an allosteric agitator can be defined as follows: (i) An agitator is a structurally labile element that undergoes incessant opening/closing fluctuations. (ii) The open state of the agitator destabilizes adjacent noncovalent contacts. (iii) Coupling of the agitator to dynamically linked residues allows the propagation of conformational perturbations in a domino-like fashion, ultimately affecting the structure/dynamics of a remote protein region (e.g., a target binding site). (iv) Allosteric effectors can block signals emanating from the agitator by stabilization (rigidification) of elements along the propagation pathway.

In future work, it will be interesting to determine if similar agitator/blocking scenarios also apply to other classes of allosteric proteins. The combined MD and HDX/MS strategy applied here should be well suited for endeavors of this type.

Acknowledgement. We thank Kathryn R. Barber for preparation of protein samples.

Supporting Information. Figure S1: S100A11 peptic digestion map; Figure S2: S100A11 sequence comparison; Figure S3: RMSD plots; Figure S4: Inter-atomic distances for all four MD conditions; Figure S5: H-bonding patterns; Figure S6: [Ca4 S100] replicate trajectory data; Figure S7: Distances for the initial 170 ns time window of three apo-S100 MD runs; Figure S8: HDX/MS kinetic plots; Figure S9: HDX/MS data mapped to protein structures.

References

- (1) Perutz, M. F. *Annu. Rev. Physiol.* **1990**, *52*, 1-25.
- (2) Schirmer, T.; Evans, P. R. *Nature* **1990**, *343*, 140-145.
- (3) Schwartz, T. W.; Hubbell, W. L. *Nature* **2008**, *455*, 473-474.
- (4) Monod, J.; Wyman, J.; Changeux, J. P. *J. Mol. Biol.* **1965**, *12*, 88-&.
- (5) Koshland, D. E.; Nemethy, G.; Filmer, D. *Biochemistry* **1966**, *5*, 365-&.
- (6) Cui, Q.; Karplus, M. *Protein Sci.* **2008**, *17*, 1295-1307.
- (7) Gui, D. Y.; Lewis, C. A.; Vander Heiden, M. G. *Sci. Signal.* **2013**, *6*.
- (8) De Smet, F.; Christopoulos, A.; Carmeliet, P. *Nat. Biotechnol.* **2014**, *32*, 1113-1120.
- (9) Dror, R. O.; Green, H. F.; Valant, C.; Borhani, D. W.; Valcourt, J. R.; Pan, A. C.; Arlow, D. H.; Canals, M.; Lane, J. R.; Rahmani, R.; Baell, J. B.; Sexton, P. M.; Christopoulos, A.; Shaw, D. E. *Nature* **2013**, *503*, 295-+.
- (10) Cooper, A.; Dryden, D. T. F. *Eur. Biophys. J. Biophys. Lett.* **1984**, *11*, 103-109.
- (11) Motlagh, H. N.; Wrabl, J. O.; Li, J.; Hilser, V. J. *Nature* **2014**, *508*, 331-339.
- (12) Sowole, M. A.; Simpson, S. A.; Skovpen, Y. V.; Palmer, D. R. J.; Konermann, L. *Biochemistry* **2016**, *55*, 5413-5422.
- (13) Kern, D.; Zuideweg, E. R. P. *Curr. Op. Struct. Biol.* **2003**, *13*, 748-757.
- (14) Boehr, D. D.; Nussinov, R.; Wright, P. E. *Nat. Chem. Biol.* **2009**, *5*, 789-796.
- (15) Nussinov, R.; Tsai, C. J. *Trends Pharmacol. Sci.* **2014**, *35*, 256-264.
- (16) Boulton, S.; Akimoto, M.; Selvaratnam, R.; Bashiri, A.; Melacini, G. *Sci Rep* **2014**, *4*, 7306.
- (17) Malherbe, P.; Kratochwil, N.; Knoflach, F.; Zenner, M. T.; Kew, J. N. C.; Kratzeisen, C.; Maerki, H. P.; Adam, G.; Mutel, V. *J. Biol. Chem.* **2003**, *278*, 8340-8347.
- (18) Suel, G. M.; Lockless, S. W.; Wall, M. A.; Ranganathan, R. *Nat. Struct. Biol.* **2003**, *10*, 59-69.
- (19) Villali, J.; Pontiggia, F.; Clarkson, M. W.; Hagan, M. F.; Kern, D. *J. Mol. Biol.* **2014**, *426*, 1554-1567.
- (20) Shi, L.; Kay, L. E. *Proc. Natl. Acad. Sci. U.S.A.* **2014**, *111*, 2140-2145.
- (21) Rivalta, I.; Sultan, M. M.; Lee, N. S.; Manley, G. A.; Loria, J. P.; Batista, V. S. *Proc. Natl. Acad. Sci. U. S. A.* **2012**, *109*, E1428-E1436.
- (22) Kumar, A.; Aguirre, J. D.; Condos, T. E. C.; Martinez-Torres, R. J.; Chaugule, V. K.; Toth, R.; Sundaramoorthy, R.; Mercier, P.; Knebel, A.; Spratt, D. E.; Barber, K. R.; Shaw, G. S.; Walden, H. *Embo J.* **2015**, *34*, 2506-2521.
- (23) Henry, E. R.; Mozzarelli, A.; Viappiani, C.; Abbruzzetti, S.; Bettati, S.; Ronda, L.; Bruno, S.; Eaton, W. A. *Biophys. J.* **2015**, *109*, 1264-1272.
- (24) Jurica, M. S.; Mesecar, A.; Heath, P. J.; Shi, W. X.; Nowak, T.; Stoddard, B. L. *Structure* **1998**, *6*, 195-210.
- (25) McClendon, C. L.; Friedland, G.; Mobley, D. L.; Amirkhani, H.; Jacobson, M. P. *J. Chem. Theory Comput.* **2009**, *5*, 2486-2502.
- (26) Lin, M. M. *J. Am. Chem. Soc.* **2016**, *138*, 5036-5043.
- (27) Doshi, U.; Holliday, M. J.; Eisenmesser, E. Z.; Hamelberg, D. *Proc. Natl. Acad. Sci. U. S. A.* **2016**, *113*, 4735-4740.
- (28) Manley, G.; Rivalta, I.; Loria, J. P. *J. Phys. Chem. B* **2013**, *117*, 3063-3073.
- (29) Gasper, P. M.; Fuglestad, B.; Komives, E. A.; Markwick, P. R. L.; McCammon, J. A. *Proc. Natl. Acad. Sci. U. S. A.* **2012**, *109*, 21216-21222.
- (30) Rajasekaran, N.; Suresh, S.; Gopi, S.; Raman, K.; Naganathan, A. N. *Biochemistry* **2017**, *56*, 294-305.

- (31) Deredge, D.; Li, J. W.; Johnson, K. A.; Wintrode, P. L. *J. Biol. Chem.* **2016**, *291*, 10078-10088.
- (32) Donovan, K. A.; Zhu, S. L.; Liuni, P.; Peng, F.; Kessans, S. A.; Wilson, D. J. *J. Biol. Chem.* **2016**, *291*, 9244-9256.
- (33) Underbakke, E. S.; Iavarone, A. T.; Chalmers, M. J.; Pascal, B. D.; Novick, S.; Griffin, P. R.; Marletta, M. A. *Structure* **2014**, *22*, 602-611.
- (34) Sheff, J. G.; Farshidfar, F.; Bathe, O. F.; Kopciuk, K.; Gentile, F.; Tuszynski, J.; Barakat, K.; Schriemer, D. C. *Mol. Cell. Proteomics* **2017**, *16*, 428-437.
- (35) Gifford, J. L.; Walsh, M. P.; Vogel, H. J. *Biochem. J.* **2007**, *405*, 199-221.
- (36) Gross, S. R.; Sin, C. G. T.; Barraclough, R.; Rudland, P. S. *Cell. Mol. Life Sci.* **2014**, *71*, 1551-1579.
- (37) Bresnick, A. R.; Weber, D. J.; Zimmer, D. B. *Nat. Rev. Cancer* **2015**, *15*, 96-109.
- (38) Santamaria-Kisiel, L.; Rintala-Dempsey, A. C.; Shaw, G. S. *Biochem. J.* **2006**, *396*, 201-214.
- (39) Rety, S.; Osterloh, D.; Arie, J.-P.; Tabaries, S.; Seeman, J.; Russo-Marie, F.; Gerke, V.; Lewit-Bentley, A. *Structure* **2000**, *8*, 175-184.
- (40) Huang, Y. K.; Chou, R. H.; Yu, C. *J. Biol. Chem.* **2016**, *291*, 14300-14310.
- (41) Hermann, A.; Donato, R.; Weiger, T. M.; Chazin, W. J. *Front. Pharmacol.* **2012**, *3*, 67.
- (42) Gabel, M.; Chasserot-Golaz, S. *J. Neurochem.* **2016**, *137*, 890-896.
- (43) Jaiswal, J. K.; Lauritzen, S. P.; Scheffer, L.; Sakaguchi, M.; Bunkenborg, J.; Simon, S. M.; Kallunki, T.; Jäättelä, M.; Nylandsted, J. *Nat. Commun.* **2014**, *5*, 4795.
- (44) Rezvanpour, A.; Santamaria-Kisiel, L.; Shaw, G. S. *J. Biol. Chem.* **2011**, *286*, 40174-40183.
- (45) Rintala-Dempsey, A.; Rezvanpour, A.; Shaw, G. S. *FEBS* **2008**, *275*, 4956-4966.
- (46) Dempsey, A. C.; Walsh, M. P.; Shaw, G. S. *Structure* **2003**, *11*, 887-897.
- (47) Capozzi, F.; Casadei, F.; Luchinat, C. *J. Biol. Inorg. Chem.* **2006**, *11*, 949-962.
- (48) Williamson, J. R. *Nat. Chem. Biol.* **2008**, *4*, 458-465.
- (49) Nandigrami, P.; Portman, J. J. *J. Chem. Phys.* **2016**, *144*, 105101.
- (50) Fenton, A. W. *Trends Biochem. Sci.* **2008**, *33*, 420-425.
- (51) Liriano, M. A.; Varney, K. M.; Wright, N. T.; Hoffman, C. L.; Toth, E. A.; Ishima, R.; Weber, D. J. *J. Mol. Biol.* **2012**, *423*, 365-385.
- (52) Allen, B. G.; Durussel, I.; Walsh, M. P.; Cox, J. A. *Biochem. Cell Biol.* **1996**, *74*, 687-694.
- (53) Martin, S. R.; Bayley, P. M.; Brown, S. E.; Porumb, T.; Zhang, M.; Ikura, M. *Biochemistry* **1996**, *35*, 3508-3517.
- (54) Grabarek, Z. *J. Mol. Biol.* **2006**, *359*, 509-525.
- (55) Dupuis, L.; Mousseau, N. *J. Chem. Phys.* **2012**, *136*, 035101.
- (56) Scotts, C. E.; Kekenos-Huskey, P. M. *Biophys. J.* **2016**, *110*, 1052-1063.
- (57) McDowell, C.; Chen, J. L.; Chen, J. H. *J. Mol. Biol.* **2013**, *425*, 999-1010.
- (58) Markowitz, J.; Rustandi, R. R.; Varney, K. M.; Wilder, P. T.; Udan, R.; Wu, S. L.; Horrocks, W. D.; Weber, D. J. *Biochemistry* **2005**, *44*, 7305-7314.
- (59) Rintala, A. C.; Schöekess, B. O.; Walsh, M. P.; Shaw, G. S. *J. Biomol. NMR* **2002**, *22*, 191-192.
- (60) Smith, S. P.; Barber, K. R.; Dunn, S. D.; Shaw, G. S. *Biochemistry* **1996**, *35*, 8805-8814.
- (61) Rintala-Dempsey, A.; Santamaria-Kisiel, L.; Liao, Y.; Lajoie, G.; Shaw, G. S. *Biochemistry* **2006**, *45*, 14695-14705.
- (62) Naka, M.; Qing, Z. X.; Sasaki, T.; Kise, H.; Tawara, I.; Hamaguchi, S.; Tanaka, T. *Biochim. Biophys. Acta* **1994**, *1223*, 348-353.
- (63) Wales, T. E.; Fadgen, K. E.; Gerhardt, G. C.; Engen, J. R. *Anal. Chem.* **2008**, *80*, 6815-6820.

- (64) Xiao, H.; Hoerner, J. K.; Eyles, S. J.; Dobo, A.; Voigtman, E.; Mel'cuk, A. I.; Kaltashov, I. A. *Protein Sci.* **2005**, *14*, 543-557.
- (65) Abraham, M. J.; Murtola, T.; Schulz, R.; Páll, S.; Smith, J. C.; Hess, B.; Lindahl, E. *SoftwareX* **2015**, *1-2*, 19-25.
- (66) Huang, J.; MacKerell, A. D. *J. Comput. Chem.* **2013**, *34*, 2135-2145.
- (67) Jorgensen, W. L.; Chandrasekhar, J.; Madura, J. D.; Impey, R. W.; Klein, M. L. *J. Chem. Phys.* **1983**, *79*, 926-935.
- (68) Piana, S.; Lindorff-Larsen, K.; Shaw, D. E. *Proc. Natl. Acad. Sci. U.S.A.* **2013**, *110*, 5915-5920.
- (69) Berendsen, H. J. C.; Postma, J. P. M.; Vangunsteren, W. F.; Dinola, A.; Haak, J. R. *J. Chem. Phys.* **1984**, *81*, 3684-3690.
- (70) Hess, B.; Henk, B.; Berendsen, H. J. C.; Fraaije, J. G. E. M. *J. Comput. Chem.* **1997**, *18*, 1463-1472.
- (71) Essmann, U.; Perera, L.; Berkowitz, M. L.; Darden, T.; Lee, H.; Pedersen, L. G. *J. Chem. Phys.* **1995**, *103*, 8577-8593.
- (72) Hung, K.-W.; Chang, Y.-M.; Yu, C. *J. Biomol. NMR* **2012**, *54*, 211-215.
- (73) Lee, H. W.; Wylie, G.; Bansal, S.; Wang, X.; Barb, A. W.; Macnaughtan, M. A.; Ertekin, A.; Montelione, G. T.; Prestegard, J. H. *Protein Sci.* **2010**, *19*, 1673-1685.
- (74) Malik, S.; Revington, M.; Smith, S. P.; Shaw, G. S. *Proteins* **2008**, *73*, 28-40.
- (75) Creighton, T. E. *Proteins*; W. H. Freeman & Co: New York, 1993.
- (76) Kyte, J.; Doolittle, R. *J. Mol. Biol.* **1982**, *157*, 105-132.
- (77) Baldwin, R. L.; Rose, G. D. *Proc. Natl. Acad. Sci. U. S. A.* **2016**, *113*, 12462-12466.
- (78) Grdadolnik, J.; Merzel, F.; Avbelj, F. *Proc. Natl. Acad. Sci. U. S. A.* **2017**, *114*, 322-327.
- (79) Southall, N. T.; Dill, K. A.; Haymett, A. D. *J. Phys. Chem. B* **2002**, *106*, 521-533.
- (80) Skinner, J. J.; Lim, W. K.; Bedard, S.; Black, B. E.; Englander, S. W. *Protein Sci.* **2012**, *21*, 996-1005.
- (81) Persson, F.; Halle, B. *Proc. Natl. Acad. Sci. U. S. A.* **2015**, *112*, 10383-10388.
- (82) Bai, Y.; Milne, J. S.; Mayne, L.; Englander, S. W. *Proteins: Struct., Funct., Genet.* **1993**, *17*, 75-86.
- (83) Bobst, C. E.; Zhang, M.; Kaltashov, I. A. *J. Mol. Biol.* **2009**, *388*, 954-967.
- (84) Sowole, M. A.; Alexopoulos, J. A.; Cheng, Y.-Q.; Ortega, J.; Konermann, L. *J. Mol. Biol.* **2013**, *425*, 4508-4519.
- (85) Burke, J. E.; Babakhani, A.; Gorfe, A. A.; Kokotos, G.; Li, S.; Woods, V. L.; McCammon, J. A.; Dennis, E. A. *J. Am. Chem. Soc.* **2009**, *131*, 8083-8091.
- (86) Shukla, A. K.; Westfield, G. H.; Xiao, K.; Reis, R. I.; Huang, L.-Y.; Tripathi-Shukla, P.; Qian, J.; Li, S.; Blanc, A.; Oleskie, A. N.; Dosey, A. M.; Su, M.; Liang, C.-R.; Gu, L.-L.; Shan, J.-M.; Chen, X.; Hanna, R.; Choi, M.; Yao, X. J.; Klink, B. U.; Kahsai, A. W.; Sidhu, S. S.; Koide, S.; Penczek, P. A.; Kossiakoff, A. A.; Woods Jr, V. L.; Kobilka, B. K.; Skiniotis, G.; Lefkowitz, R. J. *Nature* **2014**, *512*, 218-222.
- (87) Marlatt, N. M.; Shaw, G. S. *Biochemistry* **2007**, *46*, 7478-7487.
- (88) Hvidt, A.; Nielsen, S. O. *Adv. Protein Chem.* **1966**, *21*, 287-386.
- (89) McAllister, R. G.; Konermann, L. *Biochemistry* **2015**, *54*, 2683-2692.
- (90) Anderson, J. S.; Hernandez, G.; LeMaster, D. M. *Biophys. Chem.* **2013**, *171*, 63-75.
- (91) Lockless, S. W.; Ranganathan, R. *Science* **1999**, *286*, 295-299.
- (92) Laskowski, R. A.; Gerick, F.; Thornton, J. M. *FEBS Lett.* **2009**, *583*, 1692-1698.
- (93) Conn, P. J.; Christopoulos, A.; Lindsley, C. W. *Nat. Rev. Drug Discov.* **2009**, *8*, 41-54.

Figure Captions

Figure 1. (a) Sequence of rabbit S100A11; helices and calcium binding sites are indicated; side chains involved in Ca^{2+} binding are underlined. (b) Crystal structure 1QLS³⁹ of S100A11 bound to four Ca^{2+} and two annexin peptides (Ax). (c) NMR structure of apo-S100A11 (pdb file 1NSH).⁴⁶ (d) Thermodynamic cycle, illustrating the transition between apo-S100 and $[\text{Ca}_4 \text{ S100 Ax}_2]$ along two paths. Steps 1 & 2 refer to Ca^{2+} binding followed by Ax binding. Steps 3 & 4 refer to Ax binding followed by Ca^{2+} binding. The overall equilibrium constant for complex formation is the same along both paths, implying that $K_{Ca} (C_{Ca} K_{Ax}) = K_{Ax} (C_{Ax} K_{Ca})$ such that $C_{Ca} = C_{Ax} = C$.

Figure 2. (a) 1 μs MD structure of $[\text{Ca}_4 \text{ S100A11 Ax}_2]$ (magenta) and X-ray structure (gray, 1QLS).³⁹ (b) 1 μs MD apo-S100 structure (red) and NMR structure (gray, 1NSH #5).⁴⁶ (c) Helix III/IV and III'/IV' angles. Experimental values are from pdb files 1QLS,³⁹ 2LUC,⁷² and 1NSH.⁷³ MD data were averaged over the final 0.5 μs windows of 1 μs simulation runs, and data are shown separately for subunits A and B from two independent runs for each condition. Error bars represent standard deviations.

Figure 3. 1 μs MD structures for the four simulation conditions. Structures and equilibrium arrows are arranged in accordance with Figure 1d. One subunit in each panel is grayed out to reduce clutter. Hydrophobic side chains (I, V, L, F, M, A) are displayed as sticks. Spacefill representation was used for residues constituting the D57/K32/M60/L71 “shoulder”, which is intact only in panels (a, c). Ca^{2+} and Ax are displayed in magenta. Dashed lines indicate the helix III/IV orientation, which defines whether target binding sites are open (a, c), or closed (b, d).

Figure 4. (a) 1 μ s MD structure of [Ca₄ S100]. Exposed nonpolar residues in the target binding site are highlighted in red. (b) 1 μ s MD structure of apo-S100. (c) Atoms used for tracking protein conformational dynamics. (d-i) Atom distances for [Ca₄ S100]. Panels (j-o) and (p-u) display two apo-S100 runs. Dashed lines indicate target binding site closing midpoint (panels n, t).

Figure 5. Close-up views of the EF-hand calcium binding region during MD runs. (a) [Ca₄ S100] at 1 μ s. (b) [Ca₄ S100] while undergoing a structural perturbation at $t \approx 70$ ns. (c) apo-S100. Side chains comprising the D57/K32/M60/L71 shoulder, as well as those of L63 and F73 are shown as spheres. EF-hand side chains involved in calcium binding are shown as sticks, and labeled in red.

Figure 6. HDX/MS kinetics of selected segments. (a) Residues 14-17 in helix I, (b) residues 18-30 in the pseudo EF-hand, (c) residues 66-71 in the EF-hand calcium binding site, (d) residues 92-101, representing the C-terminus. Each panel contains results for four experimental conditions. Data points represent the average of three independent measurements. Standard deviations are shown as error bars. Bi-exponential fits (solid lines) were included for illustrative purposes.

Figure 7. Comparison of HDX/MS data at $t = 10$ min (round symbols, plotted vs. peptide midpoint) and MD H-bonding patterns for (a) [Ca₄ S100 Ax₂], (b) [Ca₄ S100], (c) [S100 Ax₂], and (d) apo-S100. Solid lines represent the time fraction during which backbone NH sites are H-bonded during the final 0.5 μ s of the MD simulations (data are shown for both subunits and for two independent MD runs). The H-bonding scale is inverted, such that high HDX levels are aligned with low H-bond percentages.

Figure 8. (a) Conventional allosteric mechanism, where effector loss triggers closing of a remote target binding site. Numbers 1, 2, ... refer to structural events associated with the signaling cascade. Panels (b) and (c): Generic representation of the mechanism uncovered in this study. (b) A fluctuating agitator triggers an allosteric cascade that causes binding site closure. (c) The presence of an effector blocks the cascade, such that the binding site stays open. (d) Cartoon summary of the calcium-mediated blocking mechanism in S100A11. The upper pathway results in binding site closure. In the lower pathway calcium in the EF-hand blocks signal transfer, information flow stalls, and the binding site stays open.

Figure 1

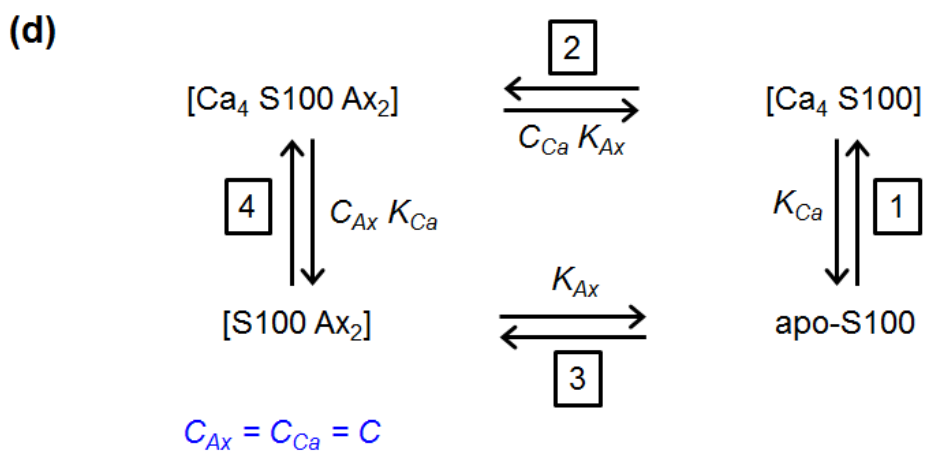
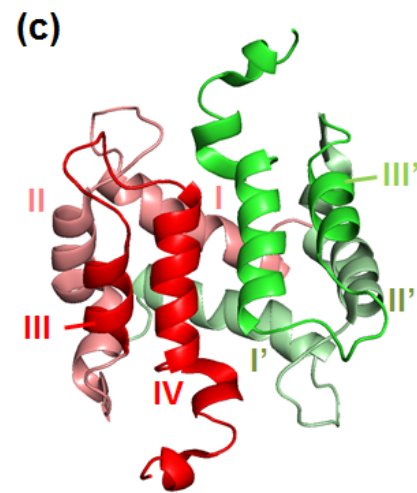
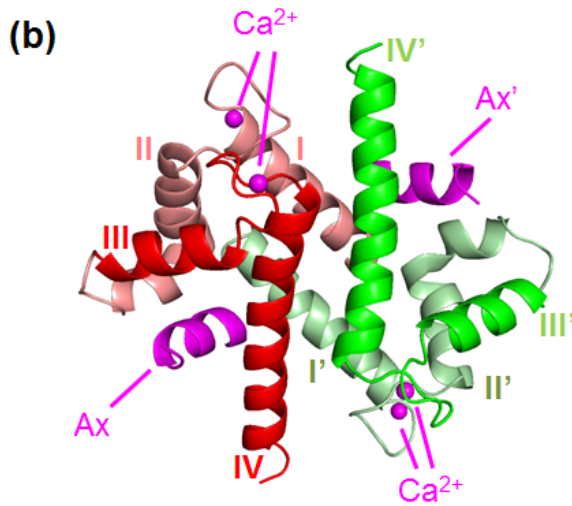
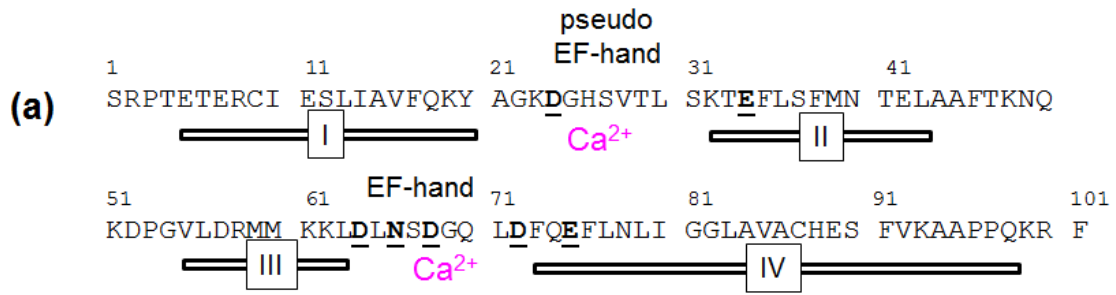


Figure 2

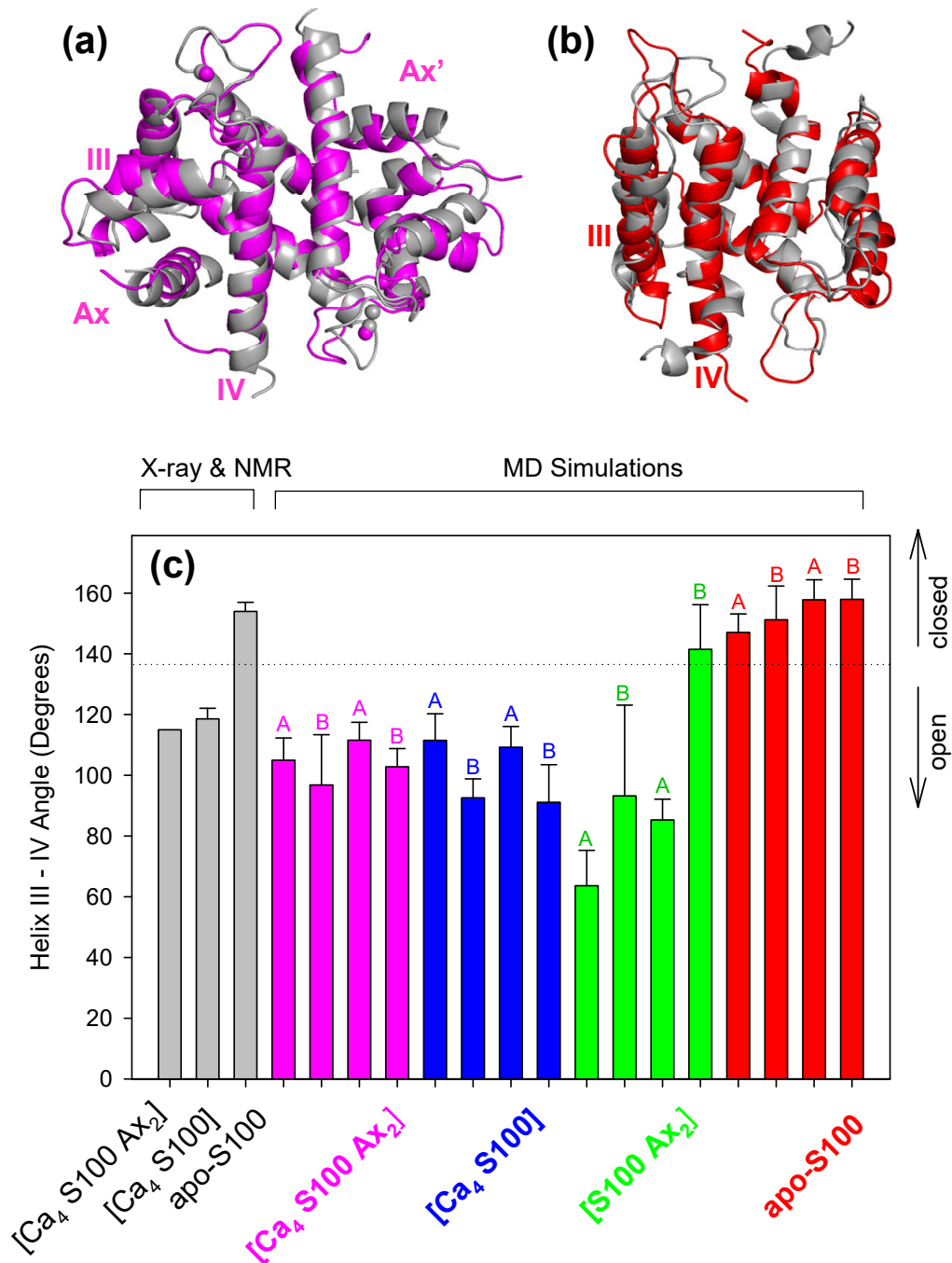


Figure 3

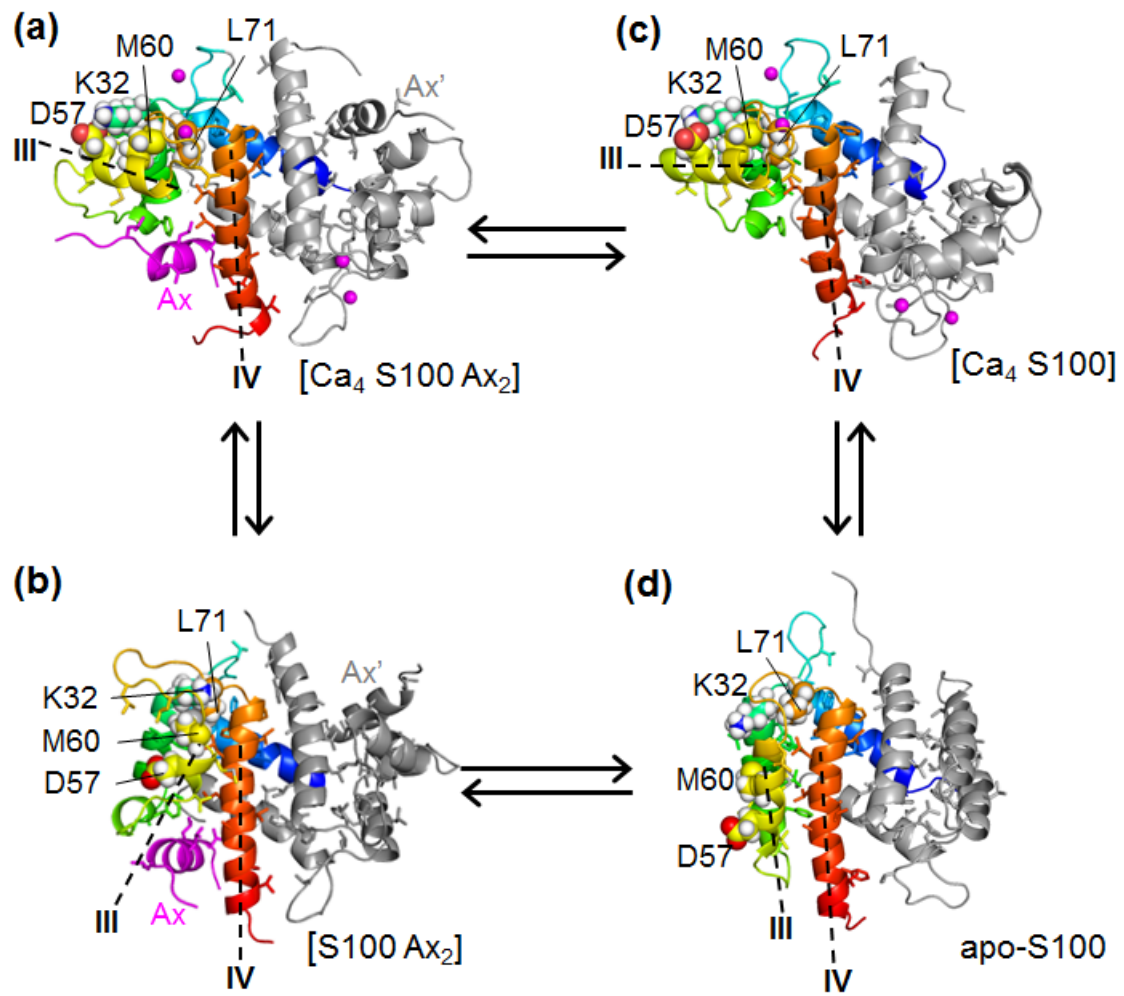


Figure 4

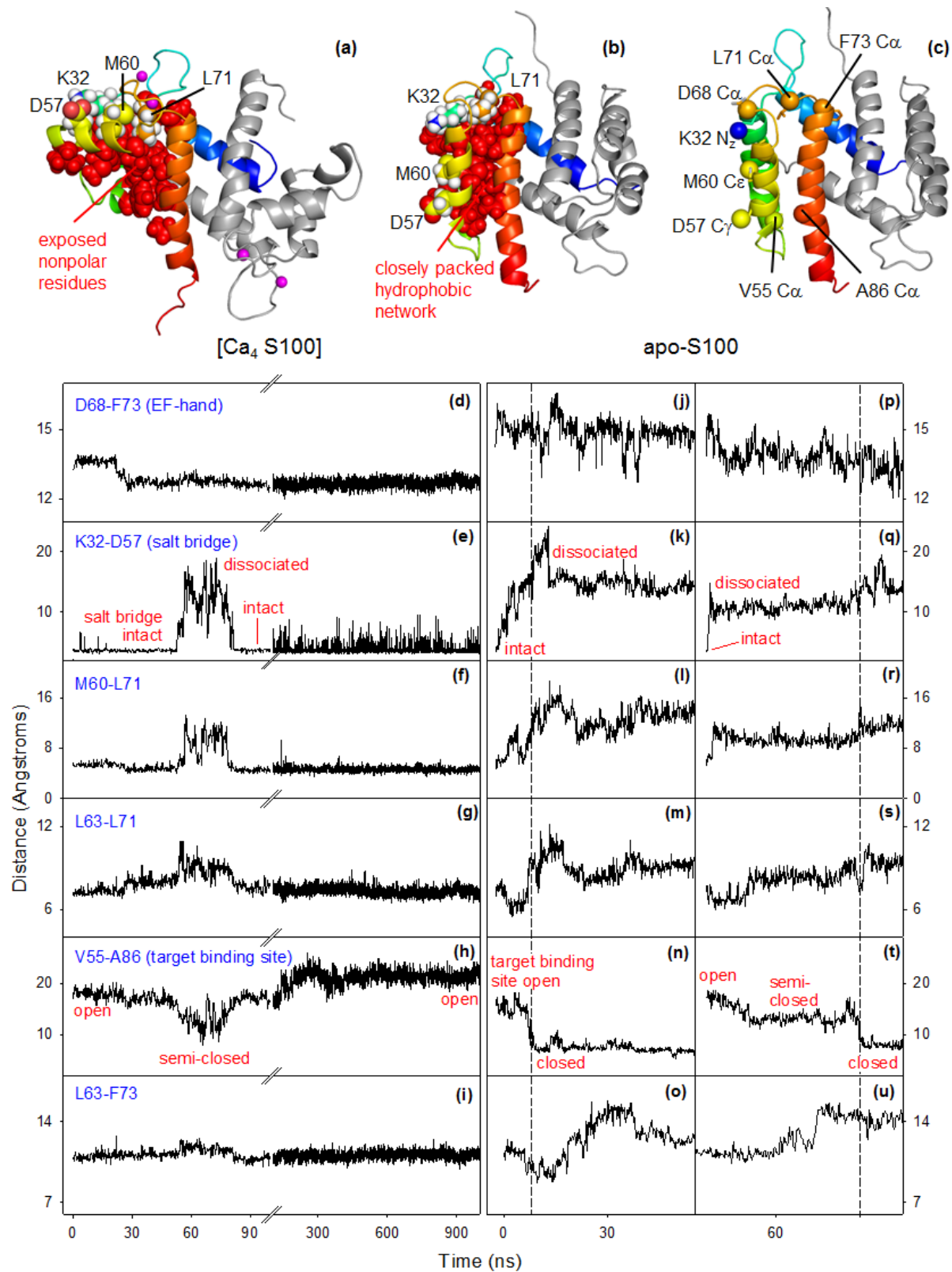


Figure 5

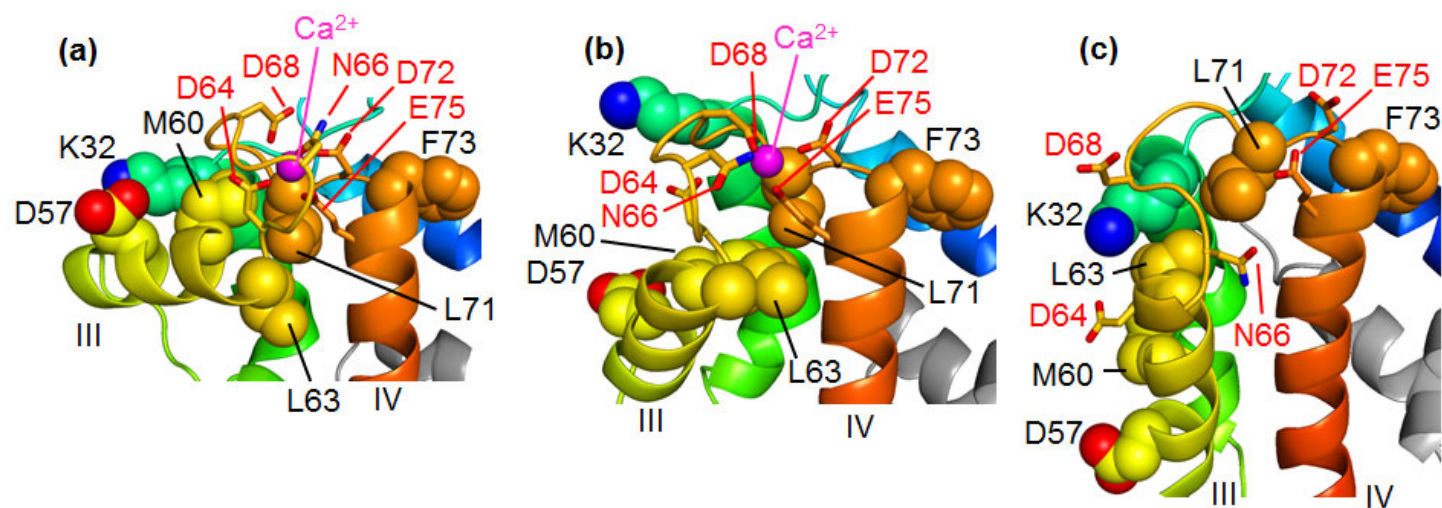


Figure 6

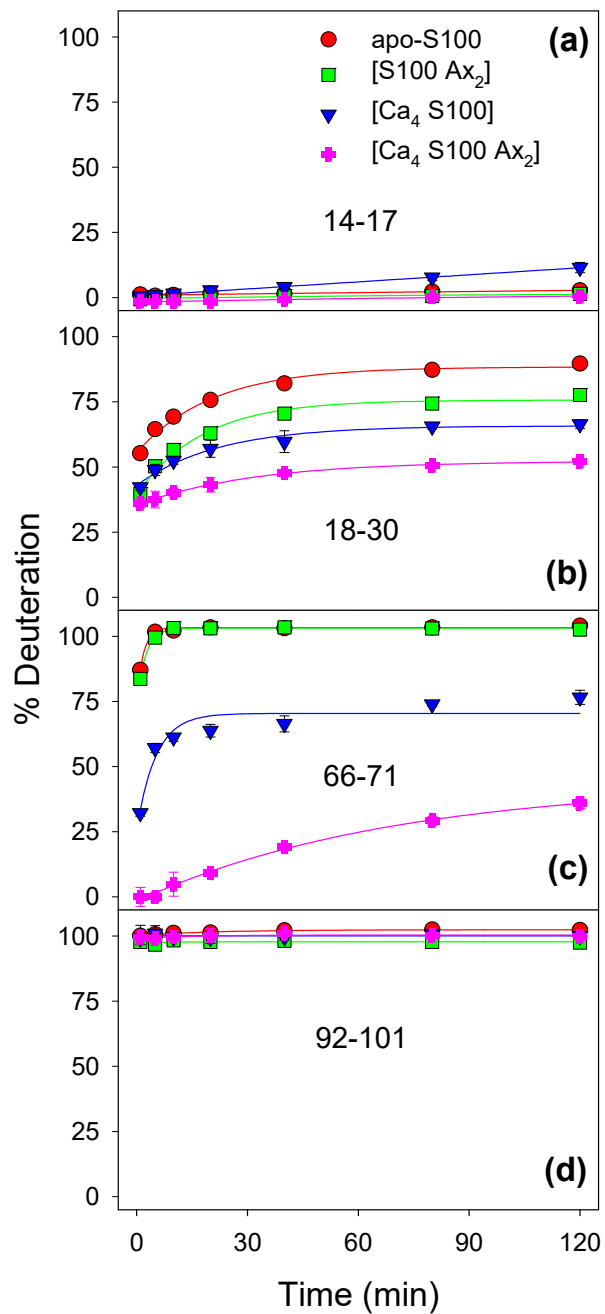


Figure 7

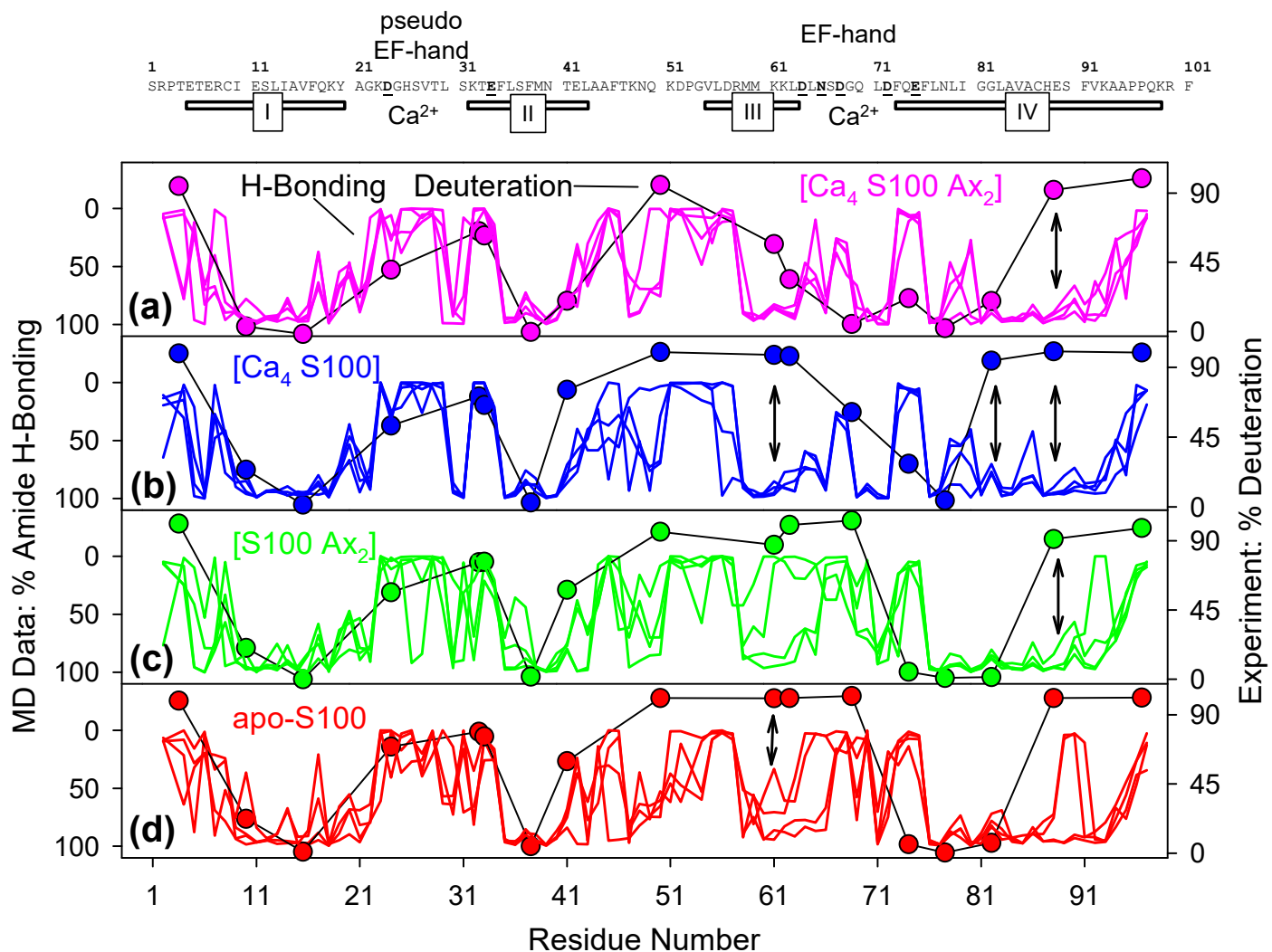
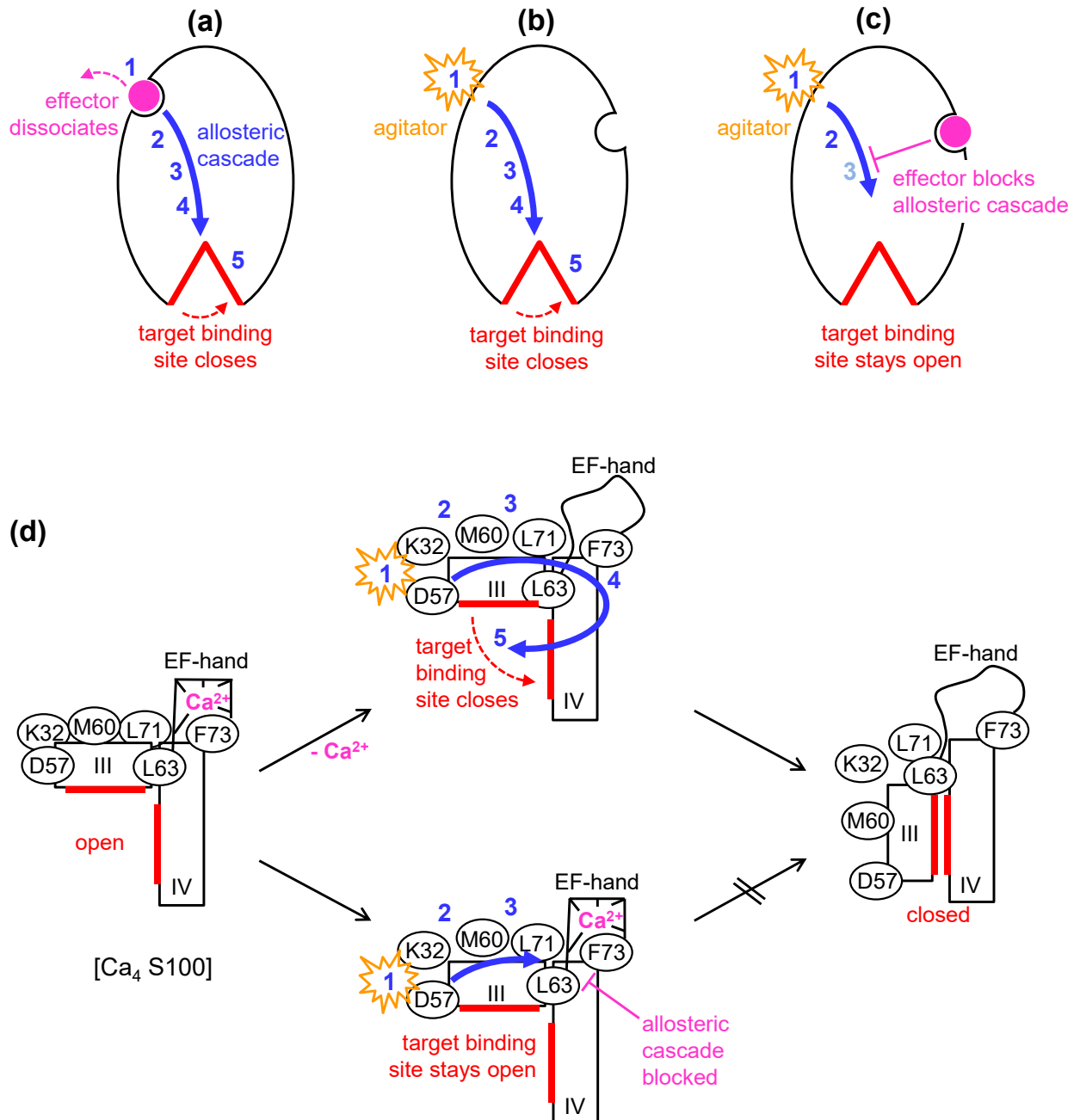


Figure 8



For Table of Contents Only

